Supplement of Geosci. Model Dev., 19, 1–25, 2026
https://doi.org/10.5194/gmd-19-1-2026-supplement

Geoscientific Model Development
Open Access
EGU

Supplement of

Representing dynamic grassland density in the land surface model ORCHIDEE r9010

Siqing Xu et al.

Correspondence to: Siqing Xu (siqing.xu@lsce.ipsl.fr)

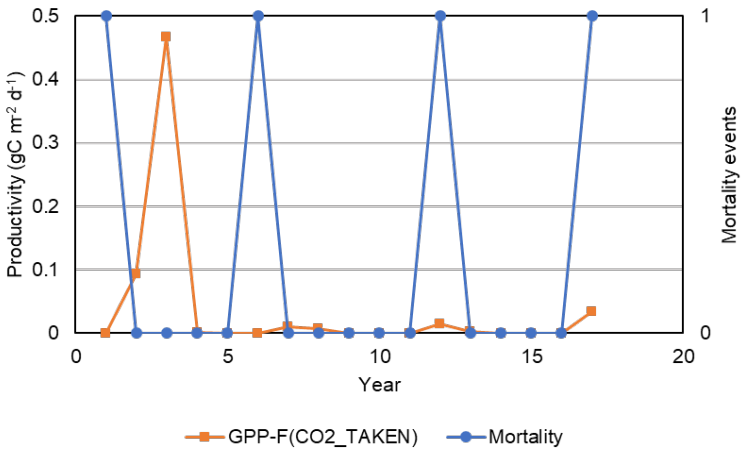

15

Figure S1. Temporal dynamics of productivity (GPP – F_{CO2_TAKEN}, orange, left axis) and mortality events (blue, right axis) over tropical C_3 grassland at (59° E, 39° N) in the fixed density approach over 17 years. Subtracting F_{CO2_TAKEN} from GPP (gross primary productivity) is intended to remove the artificial carbon uptake from the atmosphere.

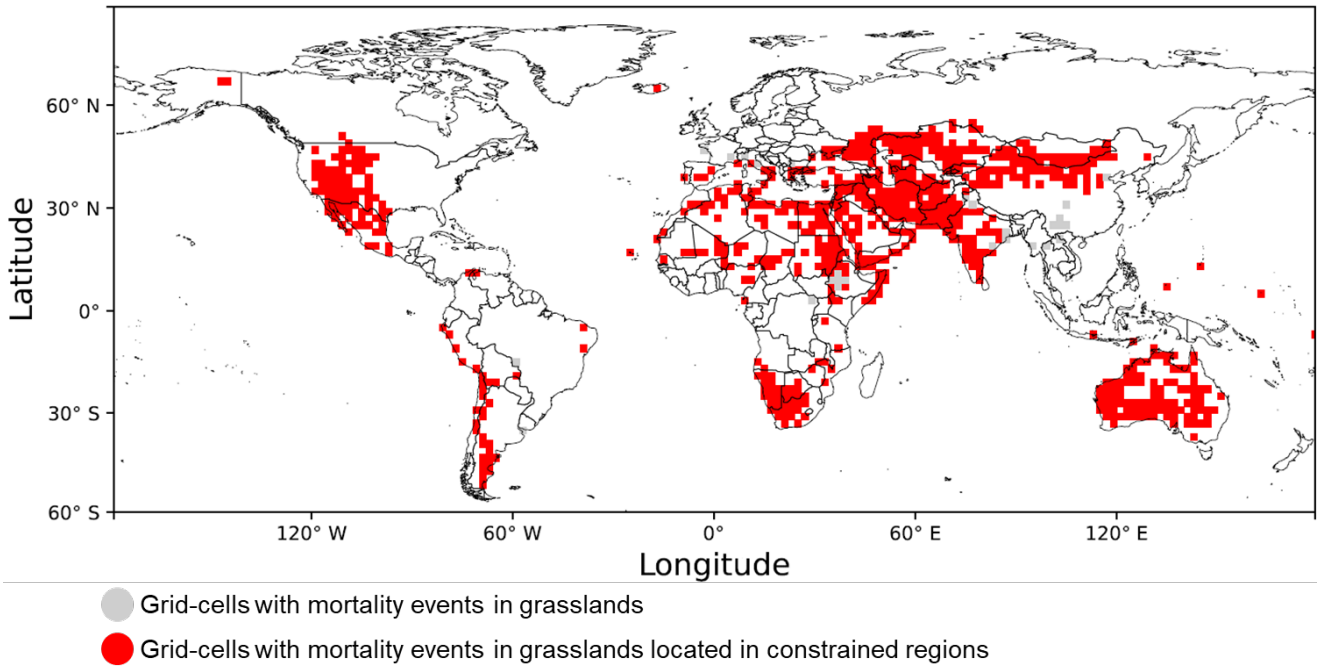

Figure S2. Spatial distribution of simulated grassland mortality artefacts. Grey squares denote grid cells where grassland mortality events occur in the simulations, while red squares indicate those located in constrained regions (hyper-arid regions, critically low LAI, or ecosystem breakdown) where grassland PFTs are unrealistically prescribed.

20

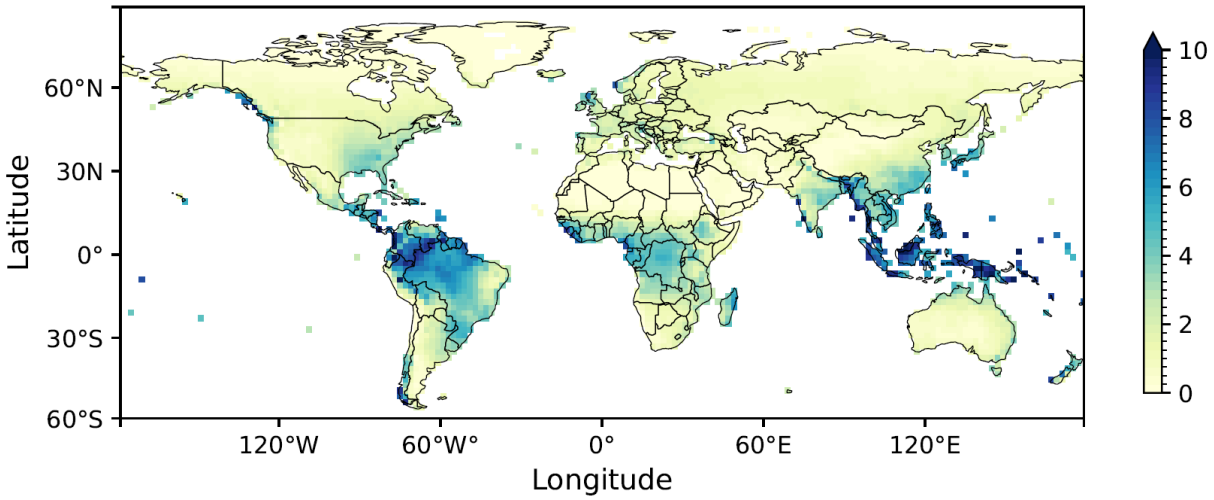

Figure S3. Global map of annual rainfall rate (mm d^{-1}) averaged over 17 years (2004-2020). The rainfall data is derived from CRU-JRA dataset as the input data.

	a	b	c	d
Water stress	Linear (by default)	Linear(by default)	Exponential, alpha=8	Exponential, alpha=8
Target of reserve + labile	(by default)	Multiply by 1.5 times	(by default)	Multiply by 1.5 times

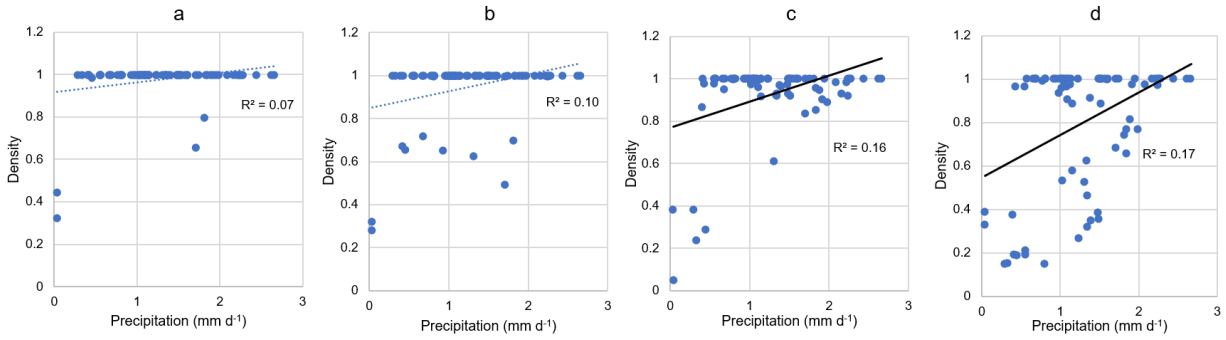

Figure S4. Regression between precipitation and grassland density for C_4 grasslands in southern Africa. The coefficient of determination (R^2) increases progressively from (a) to (d):

(a) uses the default water stress function for transpiration and the default targets for reserve and labile carbon;

(b) applies the higher targets for reserve and labile carbon while keeping the default water stress function;

(c) uses an exponential function for water stress but retains the default targets for reserve and labile carbon;

(d) combines both the exponential water stress function and the higher targets for reserve and labile carbon.

25

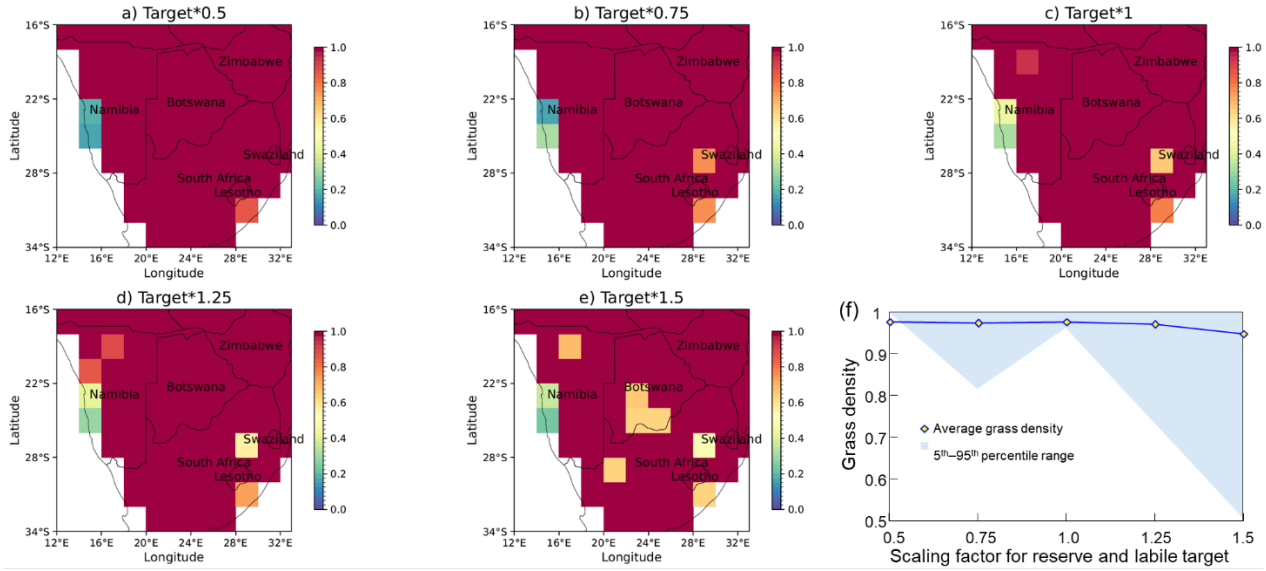

Figure S5. Grassland density (averaged from 2004 to 2020) in southern Africa C_4 grasslands in the dynamic density approach with different scaling factor for the reserve and labile carbon target. (a–e) The scaling factor was chosen as 0.5, 0.75, 1, 1.25 and 1.5. (f) The relationship between the scaling factor and grassland density, plotting the mean value across all pixels (diamonds) and the 5^{th}–95^{th} percentile range (shaded area).

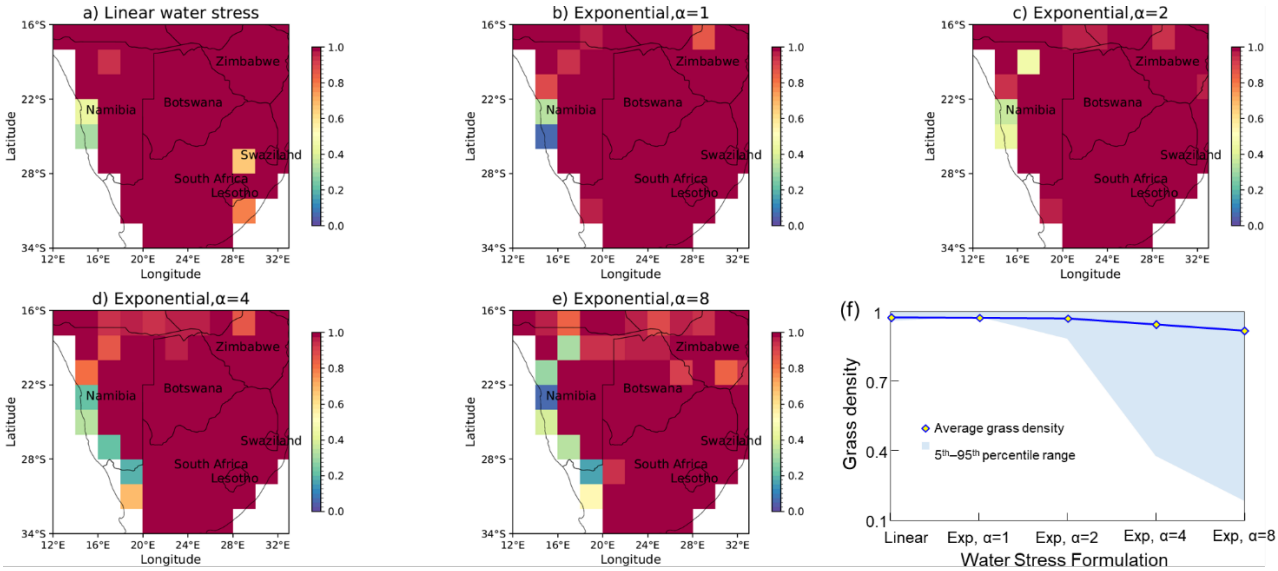

Figure S6. Grassland density (averaged from 2004 to 2020) in southern Africa C_4 grasslands in the dynamic density approach with alternative water stress formulations. (a–e) Spatial distribution of grassland density under a linear water stress formulation by default (a), and an exponential formulation with the parameter α set to 1 (b), 2 (c), 4 (d) and 8 (e). (f) Grassland density as a function of the water stress formulation, showing the mean value across all pixels (diamonds) and the 5^{th}–95^{th} percentile range (shaded area).

30

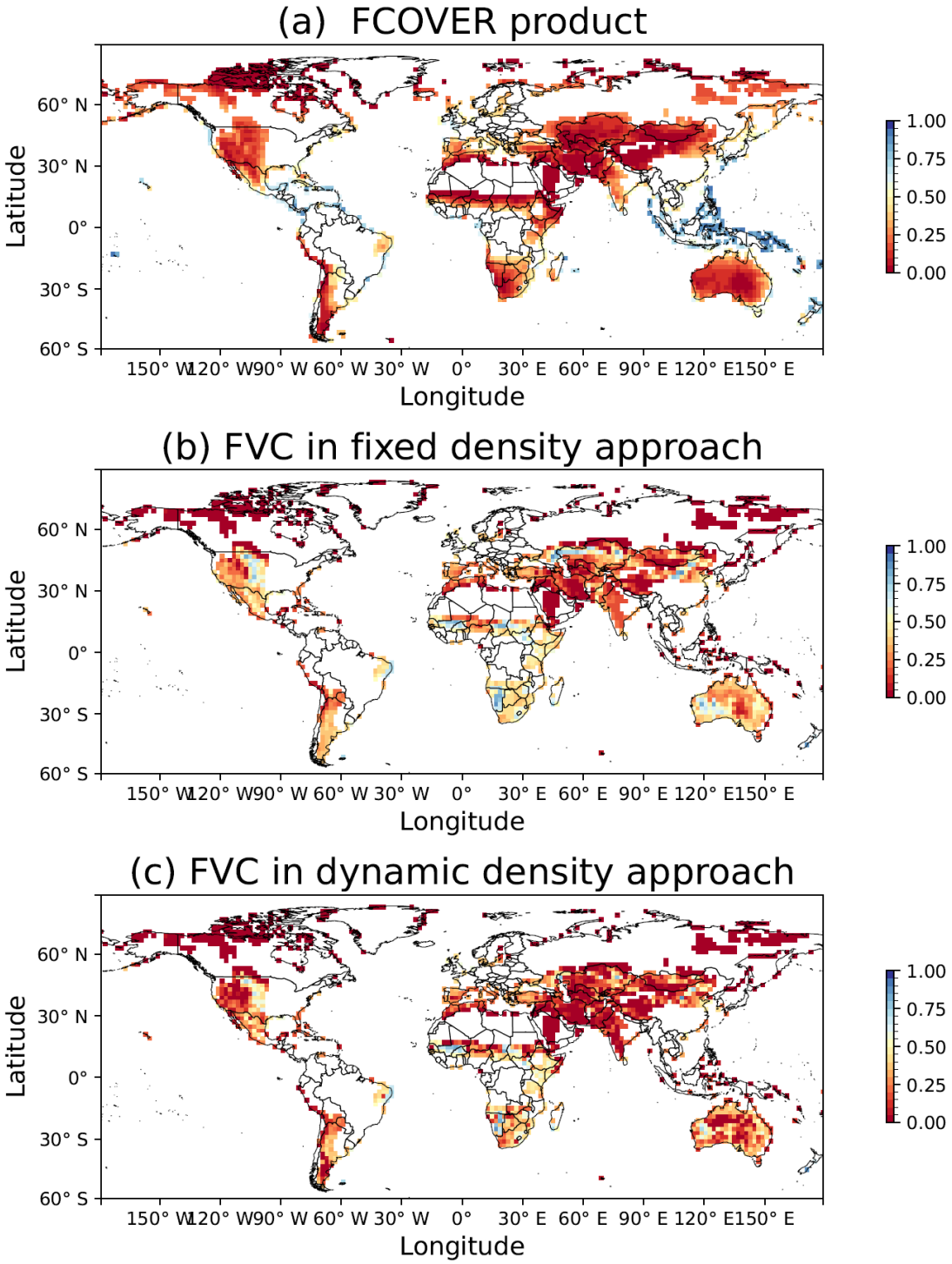

Figure S7. Fraction of vegetation cover from FCOVER product (a), simulations with fixed density approach (b) and dynamic density approach (c) in 2004.

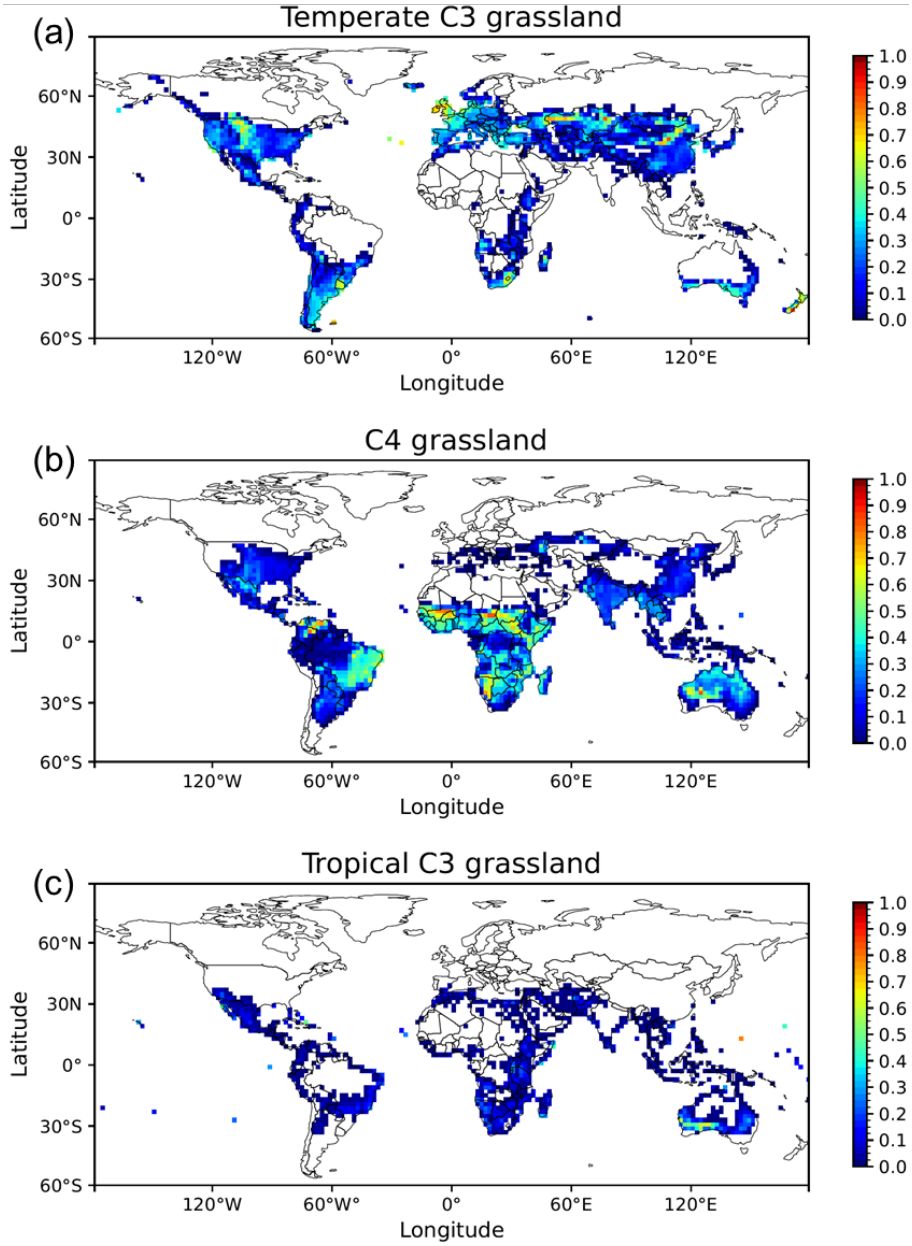

Figure S8. The global land cover map of grassland PFTs in 2004. The map was derived from the ESA CCI Land Cover dataset (Poulter et al., 2015; ESA, 2017) and used as a fixed input for all ORCHIDEE simulations.

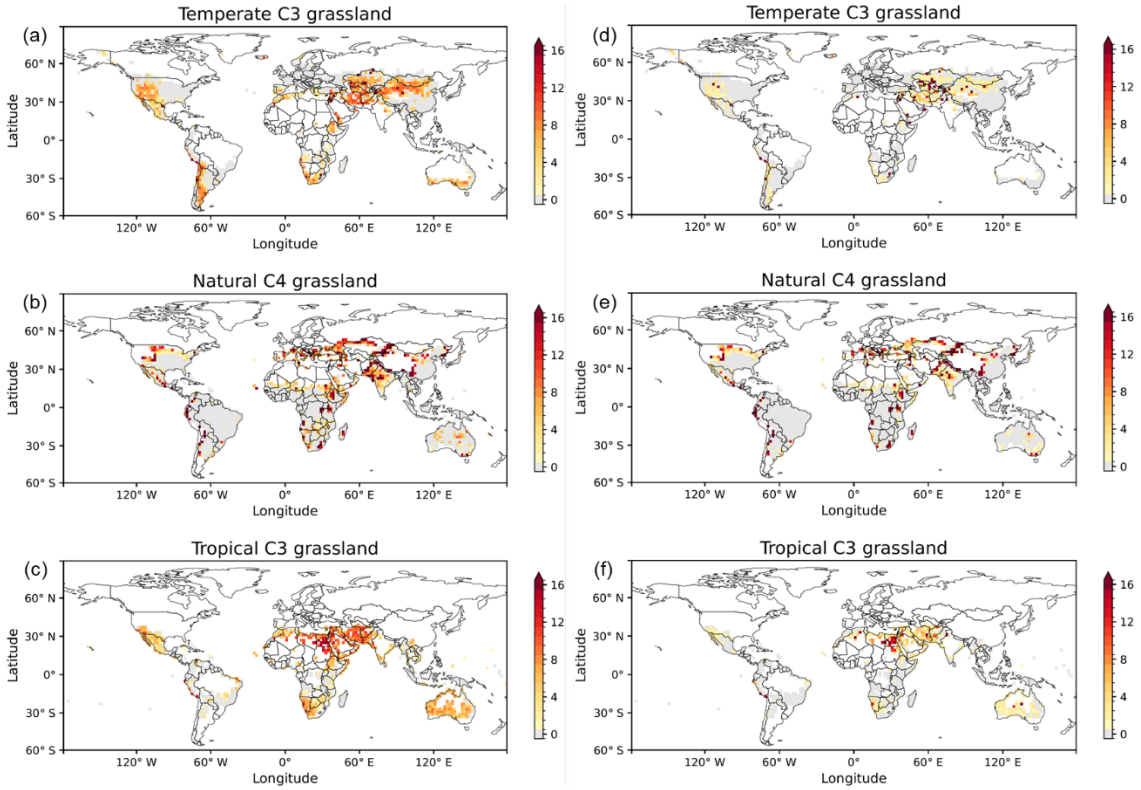

Figure S9. Frequency of individual productivity falling below the critical threshold of 10^{-4} gC per individual. Individual productivity is calculated as (GPP – $F_{CO_2\_TAKEN}$) divided by grassland density, where $F_{CO_2\_TAKEN}$ refers to the artificial carbon uptake from the atmosphere. The figure shows the number of years in which productivity falls below the survival threshold, indicating conditions insufficient to support vegetation persistence, over a 17-year period. Results are shown for three grassland types under the fixed density approach (a–c) and the dynamic density approach (d–f).

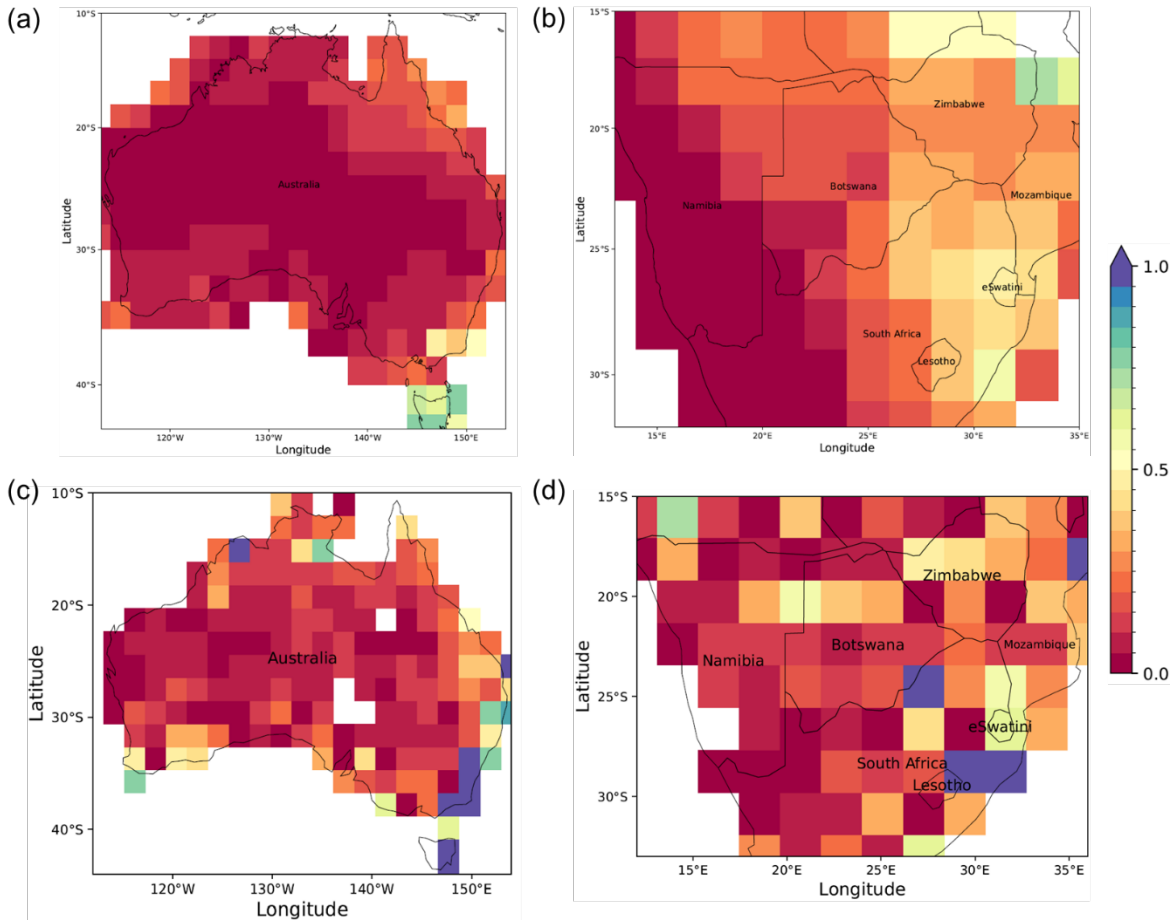

Figure S10. Mean annual LAI in grasslands in 2019 derived from the Sentinel-2 dataset and ORCHIDEE using the dynamic density approach in Australia and southern Africa. The Sentinel-2 data, initially at a 10 m resolution, has been aggregated to a 2° × 2° grid for analysis over Australia (a) and southern Africa (b). For comparison, mean annual LAI values simulated from ORCHIDEE with the dynamic density approach in 2019 are also shown for Australia (c) and southern Africa (d).

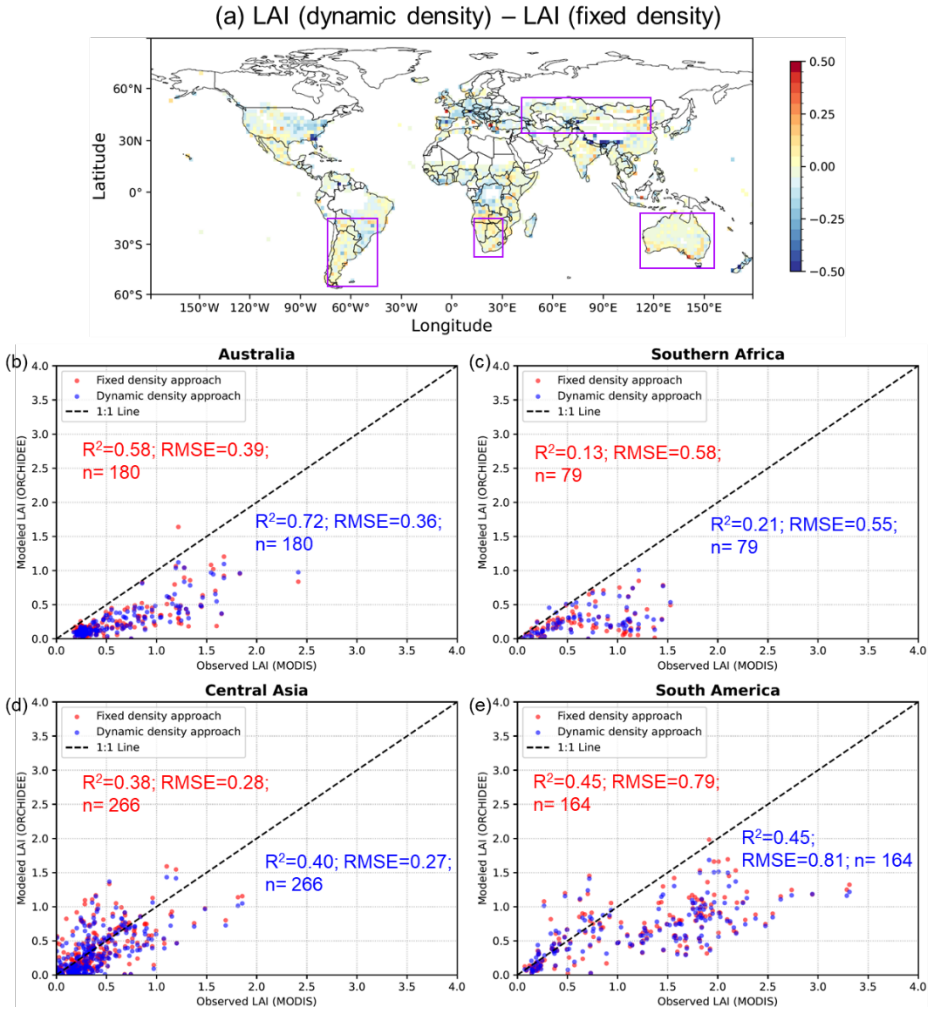

Figure S11. Comparison of simulated mean annual LAI from the fixed density and dynamic density approaches against MODIS LAI. (a) Global map of the mean annual LAI difference (Dynamic density approach − Fixed density approach). Purple boxes highlight the four representative regions: (b) Australia (113° E–155° E, 45° S–11° S), (c) southern Africa (13° E–35° E, 23° S–15° S), (d) Central Asia (41° E–119° E, 33° N–55° N), and (e) South America (75° W–45° W, 55° S–15° S). (b–e) Scatter plots comparing modelled LAI (ORCHIDEE) against observed LAI (MODIS) for each region. Red points and text correspond to the fixed density approach, while blue points and text correspond to the dynamic density approach. Statistical metrics (R^2, RMSE, and sample size n) are shown for each approach. The dashed black line is the 1:1 line. All values represent mean annual averages for the 2004–2020 period. The analysis for (b-e) was restricted to semi-arid and arid regions (based on the aridity index from Zomer et al., 2022) to ensure the comparison focused on grassland-dominated ecosystems. Both the "Observed LAI (MODIS)" (x-axis) and the "Modelled LAI (ORCHIDEE)" (y-axis) represent grassland LAI.

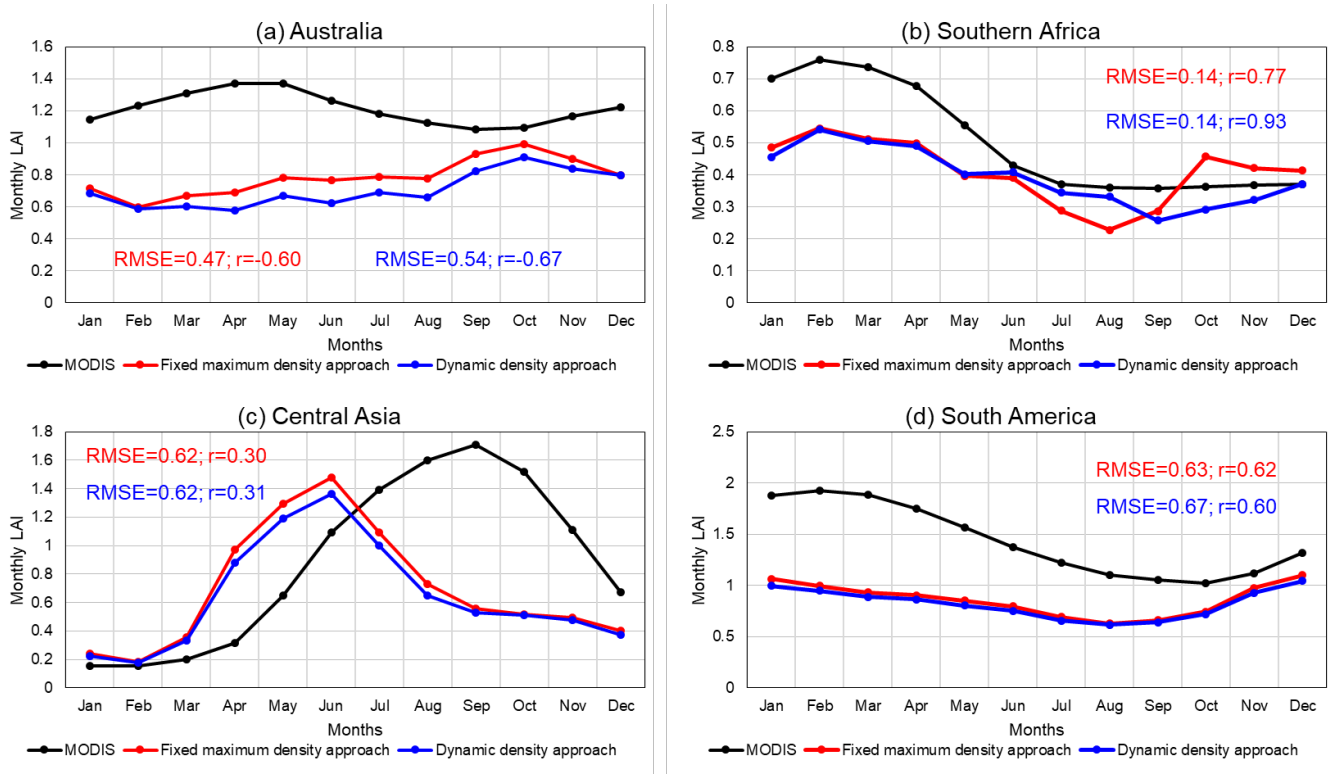

Figure S12. Average seasonal cycle of LAI, comparing MODIS observations with simulations from the fixed density (red line) and dynamic density (blue line) approaches. The comparison is shown for four representative regions: (a) Australia, (b) southern Africa, (c) Central Asia, and (d) South America. All data represent the mean monthly values, averaged over the 2004–2020 period. The analysis was restricted to semi-arid and arid regions (based on the aridity index from Zomer et al., 2022) to ensure the comparison focused on grassland-dominated ecosystems, where both MODIS and simulated LAI represent grassland LAI. Statistical metrics (Pearson's r and RMSE) for each approach against MODIS are shown in the corresponding colours.

References:

ESA (European Space Agency): Land Cover CCI Product User Guide Version 2, Tech. Rep., European Space Agency, http://maps.elie.ucl.ac.be/CCI/viewer/download/ESACCI-LC-Ph2-PUGv2_2.0.pdf, 2017.

Poulter, B., MacBean, N., Hartley, A., et al.: Plant functional type classification for earth system models: Results from the European Space Agency's Land Cover Climate Change Initiative, Geosci. Model Dev., 8, 2315-2328, https://doi.org/10.5194/gmd-8-2315-2015, 2015.

Zomer, R. J., Xu, J., and Trabucco, A.: Version 3 of the Global Aridity Index and Potential Evapotranspiration Database, Sci. Data, 9, 409, https://doi.org/10.1038/s41597-022-01493-1, 2022.